Scientific Reports

https://doi.org/10.1038/s41598-026-39328-3

Article in Press

Safety boundary protection control for distributed propulsion vehicle operating in plateau environment

Received: 21 June 2025

Accepted: 4 February 2026

Published online: 26 March 2026

Cite this article as: Dong Z., Da X., Zhang B. *et al.* Safety boundary protection control for distributed propulsion vehicle operating in plateau environment. *Sci Rep* (2026). https://doi.org/10.1038/s41598-026-39328-3

Zehong Dong, Xingya Da, Botao Zhang & Longkai Guo

Safety Boundary Protection Control for Distributed Propulsion Vehicle Operating in Plateau Environment

Zehong Dong[1], **Xingya Da**[1], **Botao Zhang**[2], **and Longkai Guo**[1,*]

[1]High Speed Aerodynamics Research Institute, China Aerodynamics Research and Development Center, Mianyang, 621000, China
[2]Taihang Laboratory, Chengdu, 610213, China
[*]675977382@qq.com

ABSTRACT

In plateau environment, aircraft encounter significant challenges stemming from low air density, strong and turbulent winds, insufficient lift and stability, as well as a tendency toward lateral–longitudinal coupling instability. To mitigate these issues, distributed propulsion technology is introduced to improve both aerodynamic and handling performance. This is combined with a boundary protection control strategy designed to enhance flight safety under complex wind conditions. First, dynamic wind tunnel tests are carried out to examine the longitudinal and lateral aerodynamic characteristics of a distributed propulsion vehicle, leading to the development of aerodynamic and dynamic models. A flight control law is then devised, in which control parameters are adaptively tuned based on the real-time flight state, and the time-domain characteristics of the resulting closed-loop system are analyzed. By systematically evaluating the flight dynamics across a wide range of initial conditions, a dynamic safety boundary is established. On this basis, a boundary protection control scheme is developed using a deep neural network. Finally, altitude flight tests are performed within the prescribed dynamic boundary, and the results validate the effectiveness of the proposed boundary protection control method.

Introduction

The take-off, landing, and flight operations in the complex wind fields of plateau regions are of considerable commercial importance but also present substantial challenges. This issue represents a multidisciplinary problem intersecting aerodynamics, control science, and systems engineering, and has attracted significant attention from relevant institutions and researchers in recent years[1–5]. According to the International Civil Aviation Organization (ICAO), airports situated above 2,438 meters are defined as plateau airports. Notably, regions such as the Qinghai–Tibet and Pamir Plateau have average altitudes exceeding 4000 meters, where air density is only about 60% of that at sea level. Moreover, wind speeds frequently exceed Force 6, accompanied by highly variable wind directions. These external disturbances considerably complicate the design of flight controllers[6–8]. Under such complex wind conditions and at comparable flight velocity and angle of attack, aircraft experience a reduction of approximately 40% in lift, thrust, and control moments. As a result, aircraft operating in these environments must exhibit exceptional lift capacity and strong wind resistance to ensure safe take-off and landing at plateau airports.

Recent advances in aviation research have confirmed that distributed propulsion vehicles (DPVs) offer multiple performance benefits-such as high lift efficiency, enhanced aerodynamic performance, and reliable operational capability-making them a promising platform for take-off and flight in plateau environments[9–11]. DPVs employ multiple small engines distributed along the wings or fuselage as the primary power source, constituting a novel aircraft architecture. Depending on the propulsion mechanism and installation arrangement, DPVs can be broadly classified into several configurations, including tilt-rotor, leading-edge propeller, wing-embedded fan, and trailing-edge embedded fan types[12–18]. Among these, the trailing-edge embedded fan configuration integrates multiple small ducted fan engines into the wing's trailing edge. This design takes advantage of the boundary layer suction effect to significantly increase wing lift and reduce drag, while maintaining low power loss. As a result, it is regarded as an effective layout for simultaneous power augmentation and drag reduction[19].

In the complex wind fields characteristic of plateau regions, the trailing-edge ducted fan configuration used in DPVs offers two distinct advantages. First, by utilizing the boundary layer suction effect, this configuration enables an increased lift coefficient and a reduced drag coefficient, thereby enhancing the aircraft's load-carrying capacity[20–23]. Second, the integration of an aerodynamically efficient fixed-wing design allows for greater control forces and moments, which improves both maneuverability and wind resistance. Moreover, the ducted fan engine operates at a fundamental frequency exceeding 800Hz, where high-frequency noise features limited propagation range, weak penetration ability, and rapid attenuation-attributes that contribute to favorable low-noise flight performance[24]. Based on these advantages, the trailing-edge ducted fan DPV is selected

in this study as the flight test platform for operations in the complex wind field environments of high-altitude plateaus.

However, it should be noted that the ducted fan DPV represents a complex systems engineering challenge, marked by strong coupling among the control system, aerodynamics, and propulsion system. These interrelated factors present considerable difficulties that may lead to instability or stall under the demanding conditions of high-altitude plateaus[25–28]. Moreover, flight safety is continually threatened by asymmetric flight conditions, which can arise from various sources such as engine failure in multi-engine aircraft, asymmetric payload distribution, airframe damage, or the effects of environmental wind fields[29–31]. In response, numerous researchers have explored control strategies for distributed propulsion vehicles, including PID control, state-space control, and dynamic inversion control[32–38].

While existing research on PID, state-space, and dynamic inverse controllers has greatly contributed to distributed propulsion control, several limitations emerge when these methods are applied in high-altitude plateau environments-characterized by strong turbulence and low air density. First, although many model-based advanced controllers achieve high precision, they rely heavily on accurate nonlinear dynamic models. The strong coupling among aerodynamics, propulsion, and control in DPVs under severely turbulent conditions is extremely difficult to model with high fidelity. As a result, performance degradation caused by model uncertainties and unmodeled disturbances remains a major concern. More critically, conventional control schemes primarily focus on reference tracking and stability, often lacking an integrated real-time framework for proactive flight envelope protection. In plateau regions, where crosswinds and maneuver coupling cause the safe flight envelope to contract and shift significantly, tracking performance alone is insufficient. The key challenge lies in preventing the aircraft from approaching stall or loss-of-control boundaries-an aspect not explicitly addressed by these controllers. Boundary protection control offers a potential solution by evaluating the flight safety margin in real time based on the distance between the current flight state and the predefined safety boundary, and implementing corresponding protection strategies. It serves as an effective approach to handling uncertain wind disturbances in high-altitude flight environments[39].

Accordingly, a control framework that integrates precise tracking with real-time adaptation to the dynamic safety boundary is critically needed. This work presents a boundary protection control strategy, supported by wind tunnel tests, to address this need and enhance the flight safety of distributed propulsion vehicles operating in the complex wind fields of high-altitude plateaus.

1 Aerodynamic Characteristics of Distributed Propulsion Verification Aircraft

The aircraft features a blended-wing-body configuration. Propellers are mounted on the inner section of the upper wing surface to exploit the boundary layer suction effect, thereby enhancing lift and reducing drag to meet the stringent performance requirements for high-altitude takeoff and landing. The wing trailing edges are equipped with flaps and ailerons, while a V-tail configuration is adopted for attitude and directional control.

To acquire accurate aerodynamic characteristics of the distributed propulsion test aircraft, a full-scale dynamic wind tunnel test was conducted in a large low-speed wind tunnel facility. Key methodological considerations-including Reynolds number effects, wind tunnel wall interference, and support system interference-were addressed to ensure the reliability and accuracy of the aerodynamic data[40,41]. The test plan encompassed typical flight conditions such as cruise, yaw under differential thrust, and banked turns. A structured grid strategy was applied to discretize these flight states. Measurements included baseline performance, control effectiveness of the V-tail and aileron surfaces, and differential thrust response, yielding aerodynamic forces and moments at critical operating points. The wind tunnel tests were performed at four inflow velocities: 25m/s, 33m/s, 42m/s, and 50m/s. The ducted fan power setting was varied among three levels: off, 45% power, and 85% power. Ambient conditions were maintained at an air density of 1.225kg/m^3 and a temperature of 15 °C, with the Reynolds number ranging from 9.4132×10^5 to 1.8826×10^6.

To investigate the influence of the ducted fan power on the longitudinal aerodynamic characteristics, force measurements were conducted in an open-jet wind tunnel. Figure 1 shows the variations of the lift coefficient C_L, residual thrust coefficient C_R, and pitching moment coefficient C_m with the angle of attack. Tests were performed at ducted fan power settings of 0 and 85%, with a freestream velocity of 25m/s, zero sideslip angle, zero V-tail rudder deflection, and all data referenced to the wind-axis coordinate system. The residual thrust coefficient is defined as $C_R = C_D - C_T$, where a negative value indicates that and the thrust coefficient C_T exceeds drag coefficient C_D, and a positive value indicates that drag coefficient exceeds thrust coefficient. In Figure 1(a), the blue curve corresponds to the lift coefficient at 0 fan power, and the black curve represents the aerodynamic coefficients at 85% power. It can be observed that for angles of attack below 18°, the lift coefficient increases nearly linearly with the angle of attack. This confirms that the proposed configuration significantly enhances the aircraft's lift generation. Furthermore, the stall angle of attack is notably increased, indicating an expansion of the flight envelope.

In order to study the influence of aileron deflection on the lateral-directional aerodynamic characteristics, wind tunnel tests were conducted on the aileron control effectiveness. The variations of the lateral force coefficient C_Y, yaw moment coefficient C_n, and roll moment coefficient C_l with the angle of attack are shown in Figure 2. The fan power input was 45%, the incoming flow speed was 42m/s, and the sideslip angle was 0. The aileron control surfaces were deflected at 5° upward on the left side

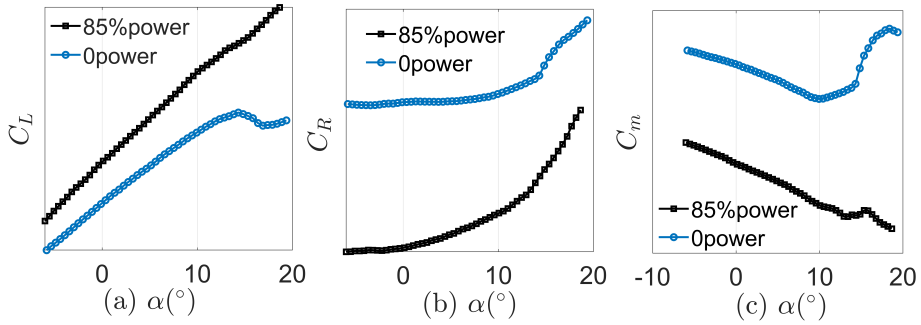

Figure 1. The longitudinal aerodynamic coefficients: (a) coefficient of lift, (b) coefficient of residual thrust, (c) coefficient of pitch moment.

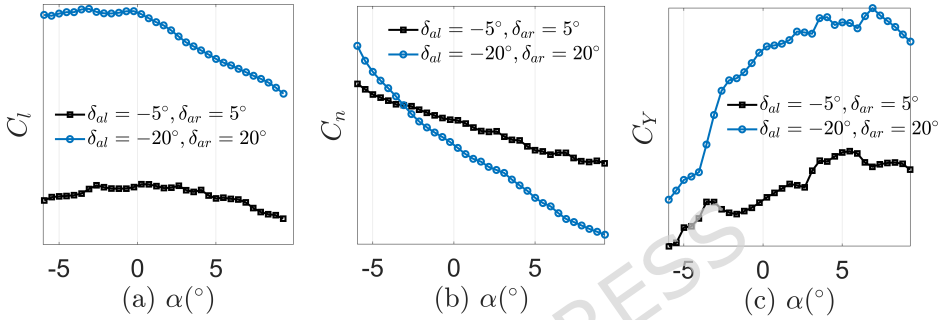

Figure 2. The differential rudder effect of aileron: (a) coefficient of rolling moment, (b) coefficient of yaw moment, (c) coefficient of lateral force.

and 5° downward on the right side ($\delta_{al} = -5^\circ, \delta_{ar} = 5^\circ$), and 20° upward on the left side and 20° downward on the right side ($\delta_{al} = -20^\circ, \delta_{ar} = 20^\circ$) respectively. It can be seen that the differential deflection of ailerons has a significant impact on the lateral force coefficient and roll moment coefficient. As the differential deflection of aileron control surfaces increases, the slope of the yaw moment coefficient curve also increases.

In order to study the influence of V-shaped tail wing deflection on the lateral-directional aerodynamic characteristics, wind tunnel tests on the aileron control effectiveness of V-shaped tail wings were carried out. The variations of the lateral force coefficient C_Y, yaw moment coefficient C_n, and roll moment coefficient C_l with the angle of attack are shown in Figure 3. The fan power input was 45%, the incoming flow speed was 42m/s, and the sideslip angle was 0. The aileron control surfaces were deflected at 5° upward on the left side and 5° downward on the right side ($\delta_l = -5^\circ, \delta_r = 5^\circ$), and 20° upward on the left side and 20° downward on the right side ($\delta_l = -20^\circ, \delta_r = 20^\circ$) respectively. It can be seen that the differential deflection of V-shaped tail wings has a significant impact on the values of the lateral force coefficient, yaw moment coefficient, and roll moment, but has a relatively small impact on the slope.

The distributed propulsion vehicle can utilize the power differential to provide yawing moment, which has stronger lateral wind resistance capability. To take advantage of the strong lateral control advantage of the distributed propulsion vehicle, a wind tunnel test with power differential was carried out. The variations of the lateral force coefficient C_Y, yaw moment coefficient C_n, and roll moment coefficient C_l with the angle of attack are shown in Figure 4. The angle of attack is 2°, the incoming flow speed is 42m/s, and the sideslip angle range is -26° to 0°. By analyzing the influence of power differential on aerodynamic parameters through varying the sideslip angle under different crosswinds conditions. Differential mode 1 represents 75% of the left power and 0% of the right power; differential mode 2 represents 68% of the left power and 20% of the right power; differential mode 3 represents 56% of the left power and 33% of the right power. It can be seen that the power differential has little influence on the lateral moment but has a significant influence on the yawing moment and rolling moment. In the design of the boundary protection control law for anti-crosswind capability, the power differential can be utilized to enhance the lateral control ability of the aircraft.

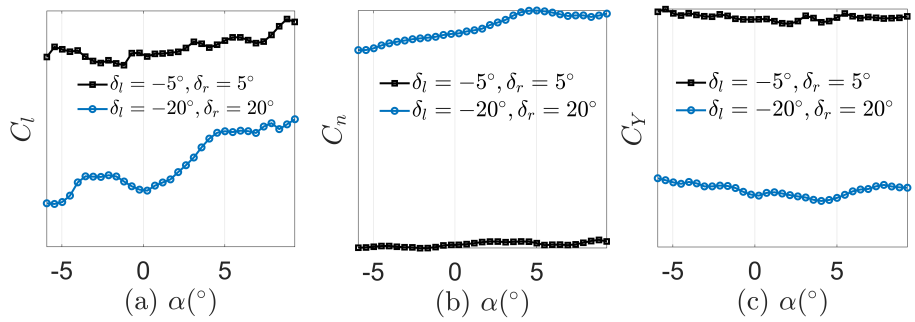

Figure 3. The rudder effect of V-tail: (a) coefficient of rolling moment, (b) coefficient of yaw moment, (c) coefficient of lateral force.

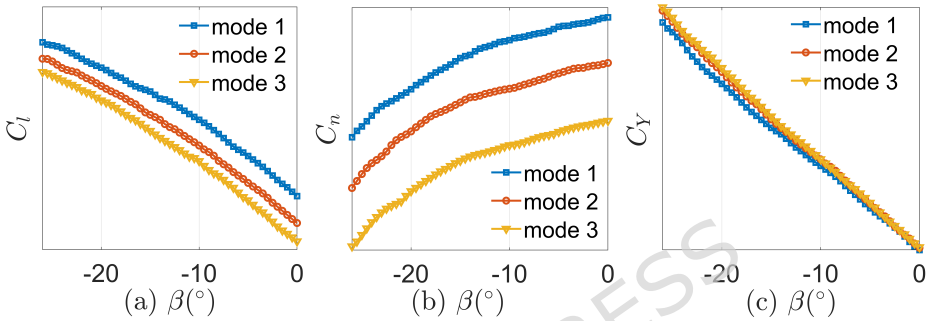

Figure 4. The lateral moment coefficient in dynamic differential mode: (a) coefficient of rolling moment, (b) coefficient of yaw moment, (c) coefficient of lateral force.

2 Dynamic Model and Control law

2.1 Dynamic model of distributed propulsion vehicle

Inspired by Kou et al[34], the six-degree-of-freedom nonlinear dynamic model is established. For clarity, the model is decomposed into the following three subsystems.

(1) Translational kinematics:

$$\begin{cases} \dot{V} = & -\frac{1}{m}C_R QS - g\sin\theta \\ \dot{\beta} = & \frac{1}{mV}\cos\beta QSC_Y + p\sin\alpha - r\cos\alpha \\ & +\frac{1}{V}g\cos\theta\sin\phi \\ \dot{\alpha} = & -\frac{1}{mV\cos\beta}QSC_L + \frac{1}{V\cos\beta}g\cos\theta\cos\phi \\ & +\frac{1}{\cos\beta}\left(-p\cos\alpha\sin\beta + q\cos\beta\right. \\ & \left.-r\sin\alpha\sin\beta\right) \end{cases} \tag{1}$$

which governs the change in velocity, primarily driven by the residual thrust and the component of gravity. Furthermore, it describes the evolution of the sideslip and angle of attack, which are critical for aerodynamic performance and stability. These equations capture the complex coupling between rotational rates, aerodynamic forces and the vehicle's attitude.

(2) Rotational Dynamics:

$$\begin{cases} \dot{p} = & \frac{I_z}{I_x I_z - I_{xz}^2}QSbC_l + \frac{I_x}{I_x I_z - I_{xz}^2}QSbC_n \\ & +\frac{I_{xz}\left(I_x - I_y + I_z\right)}{I_x I_z - I_{xz}^2}pq + \frac{I_z\left(I_y - I_z\right) - I_{xz}^2}{I_x I_z - I_{xz}^2}qr \\ \dot{q} = & \frac{QScC_m + (I_z - I_x)pr + I_{xz}\left(r^2 - p^2\right)}{I_y} \\ \dot{r} = & \frac{I_{xz}}{I_x I_z - I_{xz}^2}QSbC_l + \frac{I_x}{I_x I_z - I_{xz}^2}QSbC_n \\ & +\frac{I_{xz}\left(I_x - I_y + I_z\right)}{I_x I_z - I_{xz}^2}qr + \frac{I_x\left(I_x - I_y\right) - I_{xz}^2}{I_x I_z - I_{xz}^2}pq \end{cases} \tag{2}$$

which governs the change in angular rates. The terms involving moments of inertia represent gyroscopic cross-coupling effects. The aerodynamic moments and reference dimensions is the primary driver for vehicle maneuvering. The product of inertia accounts for the asymmetry of the vehicle.

(3) Attitude Kinematics:

$$\begin{cases} \dot{\phi} = & p + (r\cos\phi + q\sin\phi)\tan\theta \\ \dot{\theta} = & q\cos\phi - r\sin\phi \\ \dot{\psi} = & \frac{1}{\cos\theta}(r\cos\phi + q\sin\phi) \end{cases} \tag{3}$$

which describes the relationship between the body angular rates and the time derivatives of the Euler angles.

The specific meanings of the symbols in the above model are as follows: $V, \beta, \alpha, p, q, r, \phi, \theta, \psi$ represent the velocity, sideslip angle, angle of attack, roll rate, pitch rate, yaw rate, roll angle, pitch angle and yaw angle of the aircraft respectively; m, Q, S, b, c, g represent the mass, dynamic pressure, wing area, wing span, wing chord and gravitational acceleration of the aircraft respectively; I_x, I_y, I_z represent the moment of inertia about the x-axis, y-axis and z-axis of the aircraft respectively, I_{xz} represents the moment of inertia product; $C_L, C_R, C_Y, C_l, C_m, C_n$ are modeled using polynomial functions of the state and control variables, a standard practice for flight dynamics modeling within a defined operational envelope[42].

$$\begin{cases} C_L = & C_L^0 + C_L^\alpha \alpha + C_L^{\delta_e}\delta_e \\ C_R = & C_R^0 + C_R^\alpha \alpha + C_R^{\delta_e}\delta_e + C_R^{\alpha^2}\alpha^2 + C_R^{\delta_e^2}\delta_e^2 \\ C_Y = & C_Y^\beta \beta + C_Y^{\delta_a}\delta_a + C_Y^{\delta_r}\delta_r \\ C_l = & \frac{C_l^p pb}{2V} + \frac{C_l^r rb}{2V} + C_l^{\delta_a}\delta_a + C_l^{\delta_r}\delta_r + C_l^{\delta_\beta}\delta_\beta \\ C_m = & \frac{C_m^V(V-V_0)}{V_0} + \frac{C_m^\alpha \alpha}{V_0} + \frac{C_m^q cq}{2V_0} + C_m^{\delta_e}\delta_e \\ C_n = & C_n^\beta \beta + C_n^{\delta_a}\delta_a + C_n^{\delta_r}\delta_r + \frac{C_n^p pb}{2V} \\ & + \frac{C_n^r rb}{2V} + \frac{I_z}{b}\sum_{i=1}^{14} N_{T,i}C_{R_i} \end{cases} \tag{4}$$

where $N_{T,i}$ represents the horizontal distance between the i-th thruster and the longitudinal axis of the aircraft, and C_{R_i} represents the residual thrust coefficient of the i-th thruster.

2.2 Design of control law

The choice of controller type for different loops is dictated by their distinct dynamic characteristics. For the pitch and roll attitude loops, which are naturally damped and require fast, stable responses, a PD controller is employed. The derivative action provides necessary damping to suppress oscillations, while the omission of an integral term prevents potential integrator windup during aggressive maneuvers and avoids introducing unnecessary complexity, as a small steady-state error in attitude is acceptable for trajectory tracking. Conversely, for velocity and heading control, which behave more like integrating processes, a PID controller is necessary. The integral action is crucial to eliminate steady-state errors caused by persistent disturbances, such as steady crosswinds, or model inaccuracies, ensuring precise tracking of these key navigation states.

The design of the velocity control law is as follows:

$$\Phi = k_V e_V + k_{Vi}\int_0^t e_V dt + \Phi_p \tag{5}$$

where $e_V = V_r - V$ is the tracking error of velocity, V_r is the reference signal of flight velocity, V is the flight velocity; k_V and k_{Vi} are velocity control parameters; Φ is the bypass fan power, and Φ_p is the trim power of the bypass fan under cruise condition. The pitch angle control law is designed as:

$$\delta_e = k_\theta e_\theta - k_q q \tag{6}$$

where $e_\theta = \theta_r - \theta$ represents the tracking error of pitch angle, θ_r represents the pitch angle reference signal, θ represents the pitch angle; q represents the pitch angle velocity; k_θ and k_q are respectively the pitch angle control parameters and the pitch angle velocity control parameters; δ_e represents the elevator deflection angle. The roll angle control law is designed as:

$$\delta_a = k_\phi e_\phi - k_p p \tag{7}$$

where $e_\phi = \phi_r - \phi$ represents the tracking error of roll angle, ϕ_r represents the roll angle reference signal, ϕ represents the roll angle; p represents the roll angle velocity; k_ϕ and k_p are respectively the roll angle control parameters and the roll angle velocity

Table 1. Control parameters

Parameters	V=35m/s	V=40m/s	V=45m/s	V=50m/s
k_θ	4.87	5.59	6.29	6.99
k_q	0.27	0.23	0.21	0.18
k_p	0.11	0.08	0.05	0.04
k_ϕ	0.51	0.39	0.31	0.25

control parameters; δ_a represents the deflection angle of the aileron. To avoid excessive roll angle, a roll angle protection system is designed:

$$\delta_{ac} = \begin{cases} -\phi - \frac{30}{57.3}, & if \phi < -\frac{30}{57.3}, \\ \delta_a, & if -\frac{30}{57.3} \le \phi \le \frac{30}{57.3}, \\ -\phi + \frac{30}{57.3}, & if \phi > \frac{30}{57.3} \end{cases} \tag{8}$$

where δ_{ac} represents the deflection angle of the aileron after limiting. The heading angle control law is designed as:

$$\delta_r = k_\beta e_\beta + k_{\beta i} \int_0^t e_\beta dt - k_r r \tag{9}$$

where $e_\beta = \beta_r - \beta$ represents the tracking error of sideslip angle, β_r represents the reference signal of sideslip angle, β represents the sideslip angle; r represents the yaw angular velocity; k_β, $k_{\beta i}$ and k_r represent the control parameters of sideslip angle and yaw angular velocity respectively; δ_r represents the rudder deflection angle.

To achieve good flight performance, the control parameters are inversely deduced by setting the desired damping ratio and oscillation frequency. Some of the control parameters are shown in Table 1.

Taking into account the engineering reality, the power limit of the bypass fan during the take-off run stage is set at 0.7 times the maximum power, while that during other stages is set at 0.85 times the maximum power. The range of the rudder deflection angle for the elevator and rudder is set to $[-20°, 20°]$. The block diagram of the basic control law is shown in Figure 5.

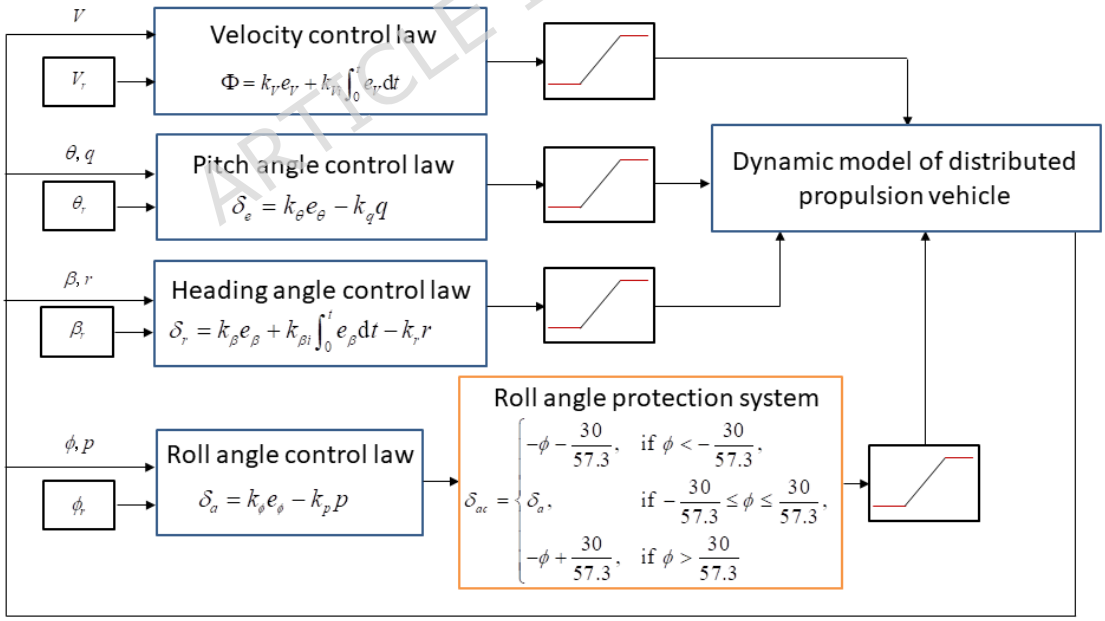

Figure 5. The structure block diagram of basic control law.

2.3 Analysis of Time Domain Response Characteristics

In order to evaluate the control performance of the aircraft, the time-domain response characteristics of the closed-loop system are analyzed. Stepping commands are given to the flight velocity and flight altitude respectively. As shown in Figure 6, the

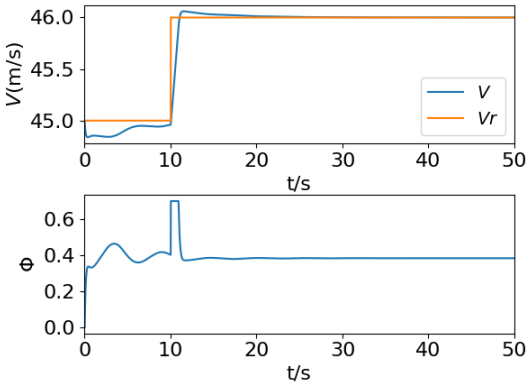

Figure 6. The flight velocity step response.

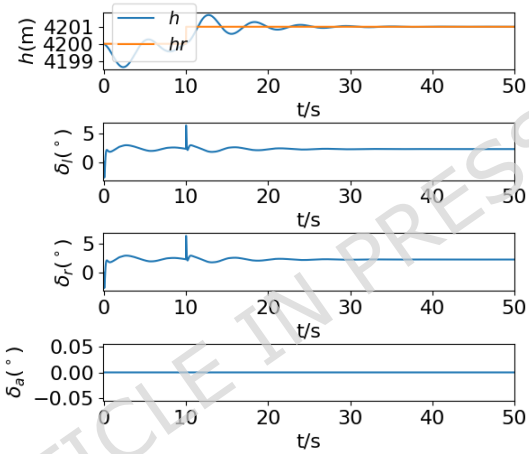

Figure 7. The flight altitude step response.

maximum overshoot of the flight velocity is 6.04%. The time required for the flight velocity to rise from the 10% of the step command to the 90% of the step command is 0.75s. The adjustment time for the error to remain within 5% of the step command is 2.3s, and the steady-state error is 0.05m/s. As shown in Figure 7, the maximum overshoot of the flight altitude is 69.1%. The time required for the flight altitude to rise from the 10% of the step command to the 90% of the step command is 1.08s. The adjustment time for the error to remain within 5% of the step command is 17.47s, and the steady-state error is 0.001m.

The aforementioned step response analysis not only verifies the basic tracking performance of the closed-loop system but also provides insight into its capability to handle in-flight uncertainties. In the complex plateau wind field, the aircraft may encounter uncertainties such as sudden wind gusts and sensor measurement noise. The step signal, as a canonical test signal, represents a severe form of disturbance due to its abrupt change. The simulation results demonstrate that the designed control system can respond rapidly to such “disturbance-like” commands and quickly dampen the transients to accurately return to the command value, as evidenced by the well-damped characteristics. The exceptionally small steady-state errors further indicate that the system possesses sufficient control authority to reject sustained external disturbances. Consequently, the controller is expected to exhibit similar stabilization and recovery capabilities when counteracting state deviations caused by actual wind disturbances and parameter uncertainties during flight.

3 Safety boundary and protection control method

3.1 The flight safety boundary

The atmospheric conditions on the plateau differ significantly from those at sea level, characterized by lower air density, stronger and highly turbulent winds, and consequently elevated flight risks. To ensure flight test safety, the flight safety boundary is

preliminarily estimated via numerical simulations. Due to the pronounced coupling between longitudinal and lateral dynamics in distributed propulsion aircraft, lateral maneuvers such as turning introduce considerable operational risks. To quantitatively assess these risks, turning maneuvers were simulated under a comprehensive set of 5386 distinct initial states, constructed from a parameter grid, as shown in Table 2, to delineate the flight safety boundary and thereby enhance the safety of subsequent flight tests.

To improve computational efficiency, strongly coupled longitudinal–lateral dynamic parameters during turning are selected as inputs. The simulation space is discretized by gridding airspeed, angle of attack, and roll angle. The initial altitude is set to 4200m, while the speed, angle of attack, and roll angle are sequentially incremented from their respective minimum values.

Table 2. The instruction set executed by vehicle

Parameters	Maximum value	Minimum value	Interval
V(m/s)	30	60	2
$\alpha(^\circ)$	-10	20	1
$\phi(^\circ)$	-40	40	1

The flight safety boundary is shown in Figure 8. The blue dots represent the stable state points. As the speed decreases, the available angle of attack range also decreases. As the roll angle increases, the available angle of attack gradually decreases, which is because after the roll angle increases, the lift of the aircraft decreases, and the aircraft is prone to stall. Due to the lower air density in high-altitude areas, at the same speed, the dynamic pressure of the aircraft is much smaller compared to sea level, and the aircraft is more likely to stall. Therefore, throughout the flight process, the amplitude of the angle of attack needs to be controlled. At high speeds, the angle of attack should not be too small either, otherwise, the descent rate will be too fast, and there is a risk of damaging the landing gear and hitting the ground.

Under crosswind conditions, the flight safety boundary will change. Figure 9 shows the flight safety boundaries of the distributed propulsion aircraft under no wind, 6m/s and 12m/s crosswind conditions. It can be seen that as the wind speed increases, the safe flight boundary becomes smaller and the stall angle of attack becomes smaller. This phenomenon is more obvious at lower speeds because crosswind intensifies the lateral longitudinal coupling, and at low speeds and large angles of attack, stall is more likely to occur. The safety boundary was derived from an evaluation of 5386 distinct initial states across a wide range of flight and crosswind conditions. This systematic analysis provides a foundational understanding of DPV behavior within the operational envelope, enhancing the generalizability of the derived protection strategy.

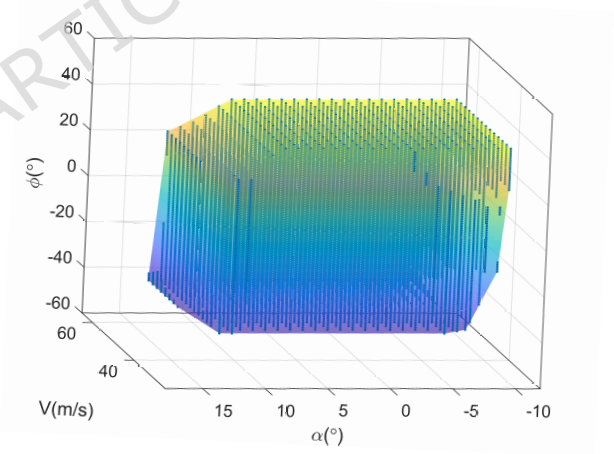

Figure 8. The flight safety boundary.

3.2 Safety boundary protection control method

In the high-altitude wind field environment, the airflow disturbance is strong and the direction changes rapidly. The flight states of tailwind, headwind and crosswind are rapidly switched, which intensifies the coupling between the lateral and longitudinal motions of the aircraft. As can be seen from the flight safety boundary in Figure 8, when the flight velocity is small and the roll angle is large, the safe angle of attack range is small. This is because as the roll angle increases, the lift coefficient keeps decreasing, and the stall speed and stall angle of attack also decrease accordingly. In the low-density and strong-wind

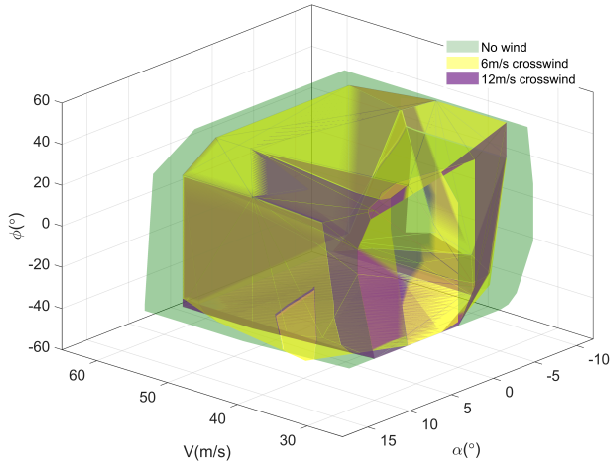

Figure 9. The safety boundary under crosswind conditions.

environment at high altitudes, the coupling of the lateral and longitudinal aerodynamic characteristics has an undeniable impact on flight safety. The schematic diagram of the influence of the cross-lateral coupling on the safety boundary is shown in Figure 10. The fundamental mechanism driving the safety boundary contraction under lateral-longitudinal coupling is the reduction of the vertical component of the aircraft's lift force during banked flight. In a coordinated turn, the total lift force L is tilted by the roll angle ϕ. The vertical component that opposes the weight G of DPV becomes $L_{\text{vertical}}=L\cos\phi$. To maintain level flight ($L_{\text{vertical}}=G$), the total lift L must increase as ϕ increases ($L=G/\cos\phi$). Since lift is a function of the angle of attack $L = C_L(\alpha)\cdot QS$, achieving a higher L requires a higher α. In the low-density environment of a plateau, where the dynamic pressure Q is already low, the DPV operates at a higher baseline α. The additional α required for turning quickly consumes the remaining margin before the stall angle of attack is reached. This interplay between roll angle, required lift, and available angle of attack is the core of the lateral-longitudinal coupling that dynamically reshapes the safety boundary.

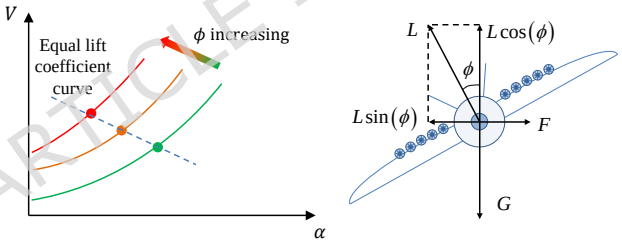

Figure 10. The safety boundary under crosswind conditions.

The flight stability is compromised under the strong wind disturbance in the plateau environment, and it is prone to induce stall with a large roll angle. The lateral and longitudinal coupling stall mechanism is very complex, involving the nonlinear strong coupling relationship among velocity, wind disturbance, and roll angle. The strong perception characteristic of the black box model of a deep learning neural network is utilized to end-to-end learn the nonlinear coupling influence laws of the flight environment and internal dynamics on the flight vehicle's motion. The input variables for the network are selected as $x = [V_w, V, \alpha, \phi, p]^T$, where V_w is the wind speed, V is the flight velocity, α is the angle of attack, ϕ is the roll angle, and p is the roll rate. The rationale is grounded in the physics of the risk of lateral-longitudinal coupling stall: V_w and V are fundamental as they determine the dynamic pressure and the relative wind state, which are the primary factors affecting the safety boundary; α and ϕ are the key state variables whose coupling directly dictates the proximity to the stall boundary, where a large ϕ reduces the effective lift and lowers the stall angle of attack; p is included as a dynamic precursor, providing the network with information about the rotational tendency of aircraft, enabling proactive protection against rapid maneuvers that could lead to a dangerous state. The output is the power differential mode, a binary decision D on whether to activate the differential thrust strategy. A single, generalized neural network model was trained using a comprehensive dataset encompassing various wind conditions. This approach allows the model to learn the universal mapping from the input state space to the safety decision, making it robust and applicable across the operational envelope without requiring retraining for specific wind scenarios. The safety boundary simulation data are extracted as training samples.

Figure 11 shows the power differential protection control model based on deep learning neural network. The network architecture is as follows: The input layer has 5 nodes, corresponding to the 5 input features. This is followed by 4 hidden layers with the number of nodes being $[128, 256, 128, 64]$. The ReLU activation function is used for all hidden layers to introduce nonlinearity, the network training parameters are shown in Table 3. The output layer consists of a single node with a Sigmoid activation function to produce a probability for the binary decision. The model was trained to minimize the Binary Cross-Entropy loss function using the Adam optimizer. To mitigate overfitting, several techniques were employed: Dropout layers with a rate of 0.2 were inserted after the first and second hidden layers; The total dataset of 5386 samples was randomly split into a training set (80%) and a validation set (20%). The validation set was used to monitor the generalization performance and to implement an early stopping criterion, which halted the training if the validation loss did not improve for 10 consecutive epochs.

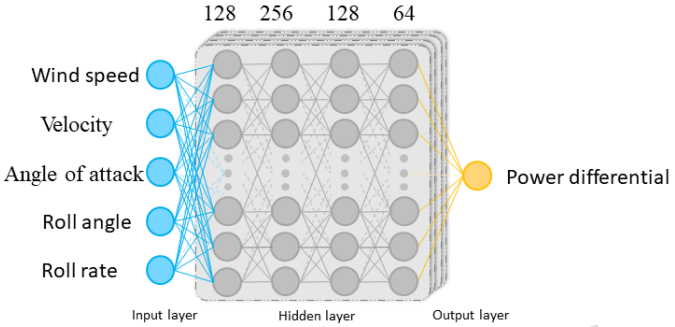

Figure 11. The control model of dynamic differential protection based on deep learning neural network.

Table 3. The training parameters of neural network

Training parameters	Maximum value
learning rate	0.001
total sample size	5386
single training batch size	128
number of iterations	1000000

The training dataset was constructed from simulation data spanning a comprehensive grid of flight states (Table 2) and wind conditions (0, 6, 12 m/s crosswind). This range is designed to be representative of the challenging but operationally relevant conditions encountered in plateau environments. While the model demonstrates robustness within this envelope, its performance in more extreme, out-of-distribution scenarios (e.g., severe gusts beyond 12 m/s, combined failures) is a subject for future research and would require an expanded training dataset.

Based on the neural network model, it is determined whether to activate the differential power response strategy. The differential power protection control system is shown in Figure 12, where $x = [V_w, V, \alpha, \phi, p]^T$, V_w represents wind speed, Ω represents the dynamic safety boundary, the neural network outputs the differential power strategy, $D := 1$ indicates that the power differential protection strategy is enabled, with a 20% power differential on both sides, while $D := 0$ meaning that the power differential protection strategy is not enabled.

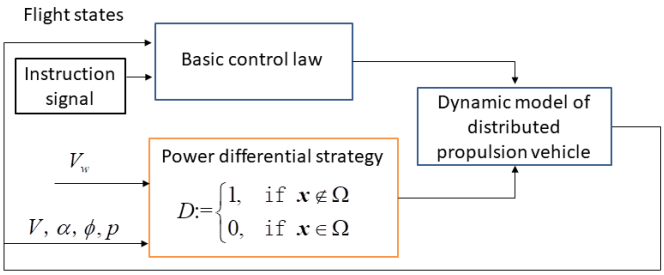

Figure 12. The dynamic differential protection control system.

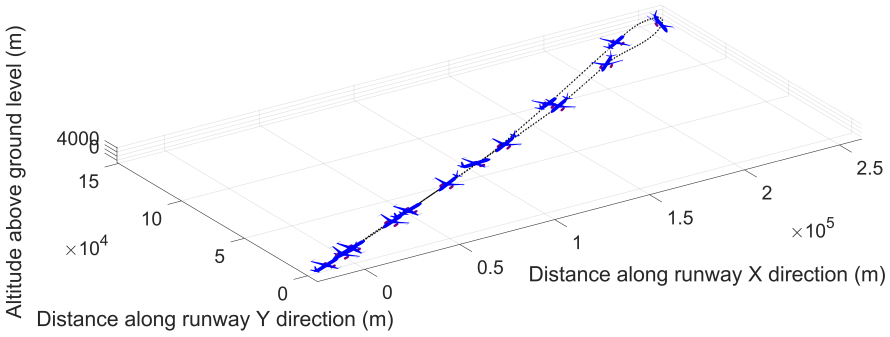

Figure 13. The flight path.

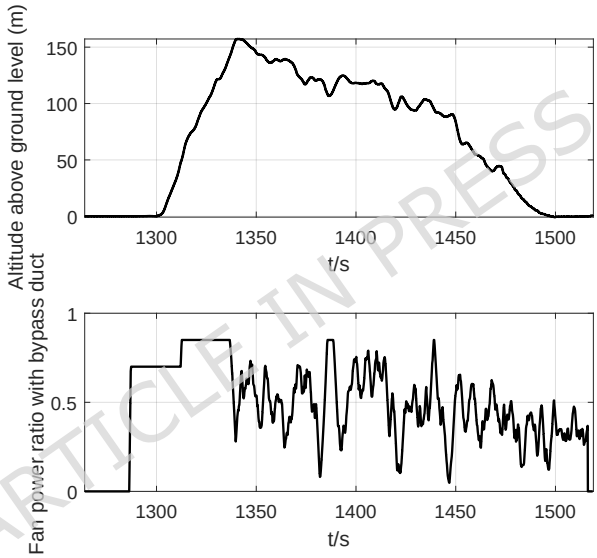

Figure 14. The relative altitude and power rate of ducted fan.

4 Flight test in plateau environment

4.1 Flight test results

The flight test was conducted at the Gesar Airport, situated at an altitude of 4068 meters. This location was selected as a representative and challenging high-altitude test environment. According to the ICAO definition (airports above 2438m), Gesar Airport is a typical plateau airport. More importantly, it is characterized by strong channel winds and significant turbulence, providing a stringent validation scenario that encompasses key challenges of plateau flight, such as low air density and complex wind fields. Successfully validating our method under these demanding conditions provides strong evidence of its potential robustness. Flight tests were carried out considering the dynamic boundary conditions for assessment. The aircraft went through stages such as taxiing, takeoff, climbing, turning, descent, and landing. The flight trajectory and some flight attitudes are shown in Figure 13.

Figures 14-18 show the flight data recorded by the flight parameter recorder. Figure 16 indicates that the aircraft began to taxi and take off around 1300 seconds after the start of the flight parameter recorder. From Figure 15, it can be seen that the aircraft began to make a 180° turn around 1380 seconds after the start of the flight parameter recorder. During the turning process, due to the effect of the roll angle protection system, the roll angle remained within the range $[-30°30°]$. A brief overshoot in the roll angle can be observed around 1420 seconds during a turning maneuver. This transient behavior is attributed

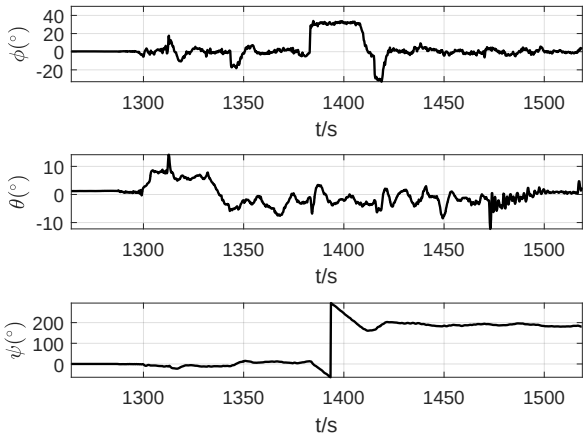

Figure 15. The roll angle, pitch angle and yaw angle.

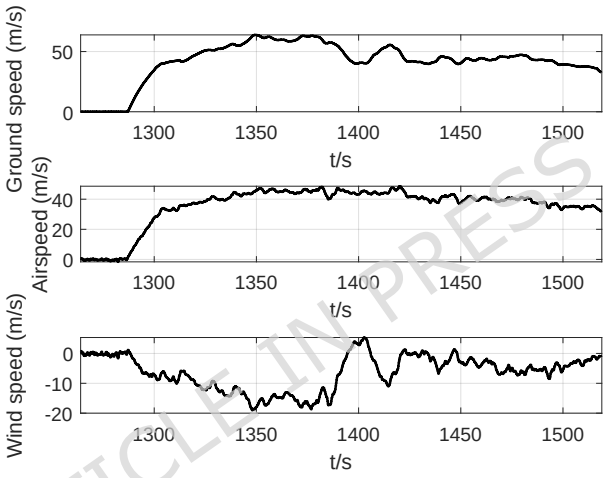

Figure 16. The ground speed, airspeed and wind speed.

to the combined effect of the actively tuned PD controller, which prioritizes rapid roll response for effective wind disturbance rejection, and the potential influence of sudden wind gusts prevalent in the plateau environment. From Figure 16, it can be seen that the maximum ground speed exceeded 50m/s, and the aircraft encountered a maximum wind speed of 19m/s, indicating that the aircraft has the ability to resist wind disturbances of level 8. The aircraft can withstand strong wind disturbances. The angle of attack is obtained through $\alpha{=}\theta - \gamma$, where γ is the climb angle. Firstly, the climb speed is obtained by differentiating the relative altitude, and then the climb angle is calculated by dividing the horizontal component of the airspeed. The calculated climb angle and angle of attack are shown in Figure 17. It can be seen that the maximum climb angle is 13°/s, corresponding to a ground speed of 45m/s and a vertical speed of 10.1221m/s. The angle of attack exhibits some oscillatory behavior during the flight. These oscillations are primarily attributed to the aircraft's active response to the strong and turbulent wind field inherent to the high-altitude plateau environment. The flight control system continuously adjusts the aircraft's attitude to maintain stability and track the desired trajectory against these gusts. Crucially, despite these oscillations, the angle of attack consistently remains within the safe boundary, and no stall condition occurred. This demonstrates that the closed-loop system possesses the necessary robustness to operate practically and safely in the challenging conditions for which it was designed. Figure 18 shows the effect of the power differential boundary protection control. Considering the influence of wind speed, flight velocity, angle of attack, roll angle, and roll angle velocity, in order to ensure flight safety, the power differential protection control model takes effect at the red dotted line, limiting the amplitude of the roll angle and avoiding the instability of longitudinal and lateral coupling under large roll angles.

4.2 Discussion and future work

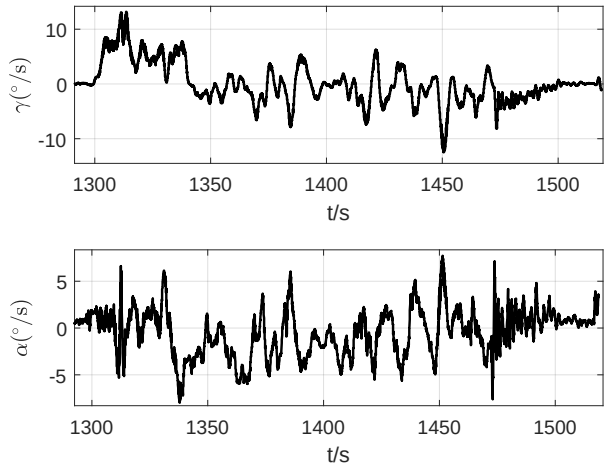

Figure 17. The climbing angle and angle of attack.

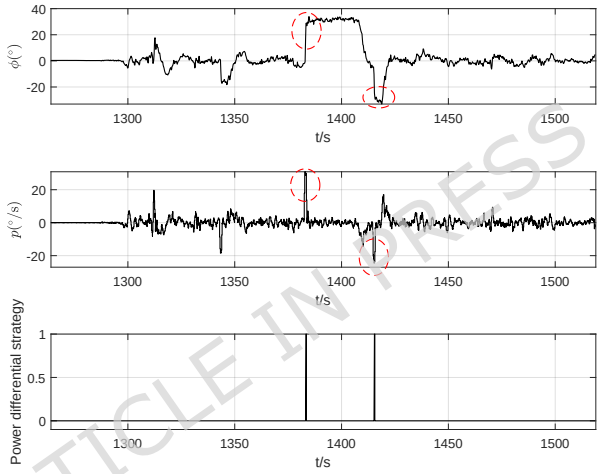

Figure 18. The boundary protection control strategy.

The successful flight test at 4068m altitude, demonstrating resilience to wind disturbances up to 19m/s, provides a critical benchmark for the practical application of distributed propulsion technology in extreme environments. When contextualized with prior research[32–38], which often lacks validation under such demanding operational conditions, this achievement highlights a significant step from simulation-based design to proven field operation. It validates the integrated PID and boundary protection control strategy as a viable approach for ensuring operational safety in the complex plateau wind field.

The control architecture in this work deliberately employs a PID-based baseline controller integrated with the proposed safety boundary protection. While advanced control techniques (e.g., model predictive control, reinforcement learning) offer potential benefits, the selection of PID was driven by key practical considerations for safety-critical flight testing: simplicity, reliability, and ease of certification. This choice serves to clearly isolate and demonstrate the efficacy of the novel dynamic boundary protection system as the primary contribution. The successful flight test confirms that this integrated approach is sufficient and effective for ensuring safety within the target operational domain defined in this study.

It is important to clarify the scope and inherent limitations of the current proof-of-concept study. The boundary protection model was trained on offline simulation data spanning a comprehensive but predefined operational envelope and a set of wind conditions representative of typical plateau challenges. Its decision is dynamically influenced by real-time inputs, notably the instantaneous wind speed, allowing adaptation to changing environmental conditions within this trained scope. However, the model is deterministic and static post-training. Consequently, its performance in more extreme out-of-distribution scenarios (e.g., severe gusts beyond 12m/s, novel failure modes), its ability to adapt to long-term system degradation, and the provision of formal analytical safety guarantees remain subjects for future investigation. The current validation-through high-fidelity simulation, extensive envelope exploration, and real-world flight testing-provides strong empirical evidence of robustness,

which is a crucial foundation for the next stages of development.

Building upon this foundation, future work will focus on enhancing the maturity, generalizability, and certifiability of the boundary protection framework through the following interconnected directions:

(1) Expanding operational envelope and robustness. Extending flight tests and data collection to a broader spectrum of meteorological conditions (e.g., more extreme wind shear, turbulence) and unseen flight regimes to iteratively expand and validate the safety envelope. Investigating integration with fault detection and diagnosis systems to handle potential propulsion failures.

(2) Enhancing adaptive and learning capabilities. Developing online and adaptive boundary estimation techniques. This includes exploring safe continual learning algorithms that can update the model from operational data to adapt to specific aircraft characteristics or degradation, and coupling the system with a high-fidelity digital twin for continuous, real-time safety boundary re-evaluation.

(3) Integrating uncertainty quantification. Incorporating uncertainty quantification methods into the model to provide confidence estimates for its decisions. This is essential for nuanced decision-making and for meeting the probabilistic safety guarantee requirements of certification authorities.

(4) Pursuing formal verification and certification. Bridging the gap between empirical validation and formal certification by: exploring integration with formally verifiable robust control inner loops; investigating methods for neural network verification and control barrier function synthesis to translate the learned boundary into a mathematically provable safe region; employing reachability analysis tools to compute forward invariant sets of the closed-loop system.

Furthermore, the core methodology presented here-using a deep learning model to identify a dynamic safety boundary and trigger proactive protection-holds significant potential for application to broader vehicle classes, such as electric vertical take-off and landing (eVTOL) aircraft operating in complex urban airscapes, or regional aircraft serving high-altitude airports. The model-agnostic learning approach allows for retraining on platform-specific data, underscoring the scalability of the framework.

5 Conclusion

This paper takes the flight test of distributed propulsion aircraft in plateau environment as the main thread. Aerodynamic data are obtained through wind tunnel tests, and the flight safety boundaries are estimated and the boundary protection control methods are proposed. The main work and conclusions are summarized as follows:

(1) The aerodynamic characteristics of distributed propulsion aircraft with power differential are analyzed. The results show that power differential can provide large yaw moment and roll moment, which can provide a basis for improving lateral control force.

(2) An aerodynamic model and a six-degree-of-freedom distributed propulsion aircraft dynamics model are established based on wind tunnel tests, and a flight controller is designed. The closed-loop system has good time-domain response characteristics.

(3) Flight dynamics boundaries are obtained through flight simulation. Boundary protection control strategies are designed based on the characteristics of plateau environment, and flight tests are completed at plateau airports to verify the effectiveness of the protection control strategies.

Funding

This work was supported by the Scientific Research Project of Taihang Laboratory under Grant A2053.

Author contributions statement

Zehong Dong and Xingya Da contributed to the study conception and design. Controller design, material preparation, data collection and analysis were performed by Zehong Dong, Botao Zhang, and Longkai Guo. All authors reviewed the manuscript.

Conflict of interest/Competing interests

The authors have no relevant financial or non-financial interests to disclose.

Ethics approval

This research does not include any human participants and Animals.

Consent for publication

All authors agree to the publication of this research.

Availability of data and materials

The datasets generated during the current study are available from the corresponding author on reasonable request.

References

1. Gohardani, A. S., Doulgeris, G. & Singh, R. Challenges of future aircraft propulsion: a review of distributed propulsion technology and its potential application for the all electric commercial aircraft. *Prog. Aerosp. Sci.* **47(5)**, 369–391 (2011).
2. Fard, M. T., He, J., Huang, H. & Cao, Y. Aircraft distributed electric propulsion technologies-a review. *IEEE Transactions on Transp. Electrification* **8(4)**, 4067–4090 (2022).
3. Gohardani, A. S. A synergistic glance at the prospects of distributed propulsion technology and the electric aircraft concept for future unmanned air vehicles and commercial/military aviation. *Prog. Aerosp. Sci.* **57**, 25–70 (2013).
4. Isikveren, A. T. *et al.* Distributed propulsion and ultra-high by-pass rotor study at aircraft level. *Prog. Aerosp. Sci.* **119(1221)**, 1327–1376 (2015).
5. Kim, H. D., Perry, A. T. & Ansell, P. J. A review of distributed electric propulsion concepts for air vehicle technology. *2018 AIAA/IEEE Electr. Aircr. Technol. Symp.* **Cincinnati, OH, USA**, 1–21 (2018).
6. Navabi, M. & Soleymanpour, S. Immersion and invariance based adaptive control of aerial robot in presence of inertia uncertainty. *2017 IEEE 4th Int. Conf. on Knowledge-Based Eng. Innov.* **Tehran, Iran**, 959–964 (2017).
7. Navabi, M., Mirzaei, H. & Davoodi, A. Optimum design of robust adaptive controller with actuator constraints. *Int. J. Control. Autom. Syst.* **18**, 2734–2741 (2020).
8. Navabi, M., Davoodi, A. & Mirzaei, H. Trajectory tracking of under-actuated quadcopter using lyapunov-based optimum adaptive controller. *Proc. Inst. Mech. Eng. Part G: J. Aerosp. Eng.* **236(1)**, 202–215 (2022).
9. Felder, J., Kim, H. & Brown, G. Turboelectric distributed propulsion engine cycle analysis for hybrid-wing-body aircraft. *47th AIAA Aerosp. Sci. Meet. including The New Horizons Forum Aerosp. Expo.* **Orlando, Florida, USA**, AIAA 2009–1132 (2009).
10. Shi, J., Zhou, J. & Wu, L. Aerodynamic investigation of a general aviation aircraft with distributed electric propulsion. *2021 IEEE Int. Conf. on Adv. Electr. Eng. Comput. Appl.* **Dalian, China**, 672–676 (2021).
11. Li, Y. Reliability analysis of distributed electric aircraft propulsion system. *2024 3rd Int. Conf. on Energy, Power Electr. Technol.* **Chengdu, China**, 1388–1391 (2024).
12. Rothhaar, P. M., Murphy, P. C. & Bacon, B. J. Nasa langley distributed propulsion vtol tilt-wing aircraft testing, modeling, simulation, control, and flight test development. *14th AIAA aviation technology, integration, operations conference* **Atlanta, GA, USA**, AIAA–2014–2999 (2014).
13. Simmons, B. M. & Murphy, P. C. Aero-propulsive modeling for tilt-wing, distributed propulsion aircraft using wind tunnel data. *J. Aircr.* **59(5)**, 1162–1178 (2022).
14. Stoll, A. M., Bevirt, J. B., Moore, M. D., Fredericks, W. J. & Borer, N. K. Drag reduction through distributed electric propulsion. *14th AIAA aviation technology, integration, operations conference* **Atlanta, GA, USA**, AIAA–2014–2851 (2014).
15. Deere, K. A. *et al.* Computational analysis of a wing designed for the x-57 distributed electric propulsion aircraft. *35th AIAA applied aerodynamics conference* **Hampton, VA, USA**, AIAA 2017–3923 (2017).
16. Kim, H. D. Distributed propulsion vehicles. *27th Int. Congr. Aeronaut. Sci.* **Nice, France**, E–17361 (2010).
17. Kerho, M. F. Aero-propulsive coupling of an embedded, distributed propulsion system. *33rd AIAA Appl. Aerodyn. Conf.* **Dallas, TX, USA**, AIAA 2015–3162 (2015).
18. Freeman, J. L. & Klunk, G. T. Dynamic flight simulation of spanwise distributed electric propulsion for directional control authority. *2018 AIAA/IEEE Electr. Aircr. Technol. Symp.* **Cincinnati, OH, USA**, 1–15 (2018).
19. He, C., Jia, Y. & Ma, D. Optimization and analysis of hybrid electric system for distributed propulsion tilt-wing uav. *IEEE Access* **8**, 224654–224667 (2020).

20. Berg, F., Palmer, J., Miller, P., Husband, M. & Dodds, G. Hts electrical system for a distributed propulsion aircraft. *IEEE Transactions on Appl. Supercond.* **25(3)**, 1–5 (2015).

21. Zhou, Y., Wu, S., Tang, Z., Jiao, Z. & Luk, P. C. Modeling and simulation of a distributed electric propulsion aircraft by modelica. *CSAA/IET Int. Conf. on Aircr. Util. Syst.* **Guiyang, China**, 1–6 (2018).

22. Weng, L., Zhang, X., Yao, T., Bu, F. & Li, H. A thrust cooperative control strategy of multiple propulsion motors for distributed electric propulsion aircraft. *World Electr. Veh. J.* **12(4)**, 199 (2021).

23. Jones, C. E., Norman, P. J., Galloway, S. J., Armstrong, M. J. & Bollman, A. M. Comparison of candidate architectures for future distributed propulsion aircraft. *IEEE Transactions on Appl. Supercond.* **26(6)**, 1–9 (2016).

24. Myose, R. *et al.* Low noise cruise efficient short take-off and landing transport vehicle study. *6th AIAA Aviat. Technol. Integration Oper. Conf.* **Wichita, Kansas, USA**, AIAA 2006–7738 (2006).

25. Stoll, A. M., Stilson, E. V., Bevirt, J. & Pei, P. P. Conceptual design of the joby s2 electric vtol pav. *14th AIAA Aviat. Technol. Integration, Oper. Conf.* **Atlanta, GA, USA**, AIAA 2014–2407 (2014).

26. Finger, D. F., Braun, C. & Bil, C. A review of configuration design for distributed propulsion transitioning vtol aircraft. *Asia-Pacific Int. Symp. on Aerosp. Technol.* **Korean Soc. for Aeronautical and Space Sciences Seoul, Korea**, 3–5 (2017).

27. Seitz, A. & Gologan, C. Parametric design studies for propulsive fuselage aircraft concepts. *CEAS Aeronaut. J.* **6**, 69–82 (2015).

28. Zhang, Y. *et al.* Optimal arrangement of electric motors for distributed electric propulsion aircraft: using nmpc and generalized benders decomposition. *IEEE Transactions on Ind. Appl.* **60(5)**, 7869–7880 (2024).

29. Predrag, S., Kosta, V. & Bosko, R. Power optimization of a single propeller airplane take-off run on the basis of lateral maneuver limitations. *Aerosp. Sci. Technol.* **72**, 553–563 (2018).

30. Predrag, S. & Bosko, R. Single propeller airplane minimal flight speed based upon the lateral maneuver condition. *Aerosp. Sci. Technol.* **49**, 239–249 (2016).

31. Predrag, S. & Bosko, R. Minimal safe speed of the asymmetrically loaded combat airplane. *Aircr. Eng. Aerosp. Technol.* **88(1)**, 42–52 (2016).

32. Huangfu, Y., Yu, T., Zhang, R., Du, Y. & Fan, A. De-centralized control for distributed electric propulsion systems in electric uavs. *2024 IEEE 19th Conf. on Ind. Electron. Appl.* **Kristiansand, Norway**, 1–6 (2024).

33. Guo, R. *et al.* Nonlinear model predictive control for the power management in hybrid distributed electric aircraft: considering aerodynamics-propulsion coupling effects. *IEEE Transactions on Transp. Electrification* **11(3)**, 7274–7286 (2025).

34. Kou, P., Wang, J. & Liang, D. Powered yaw control for distributed electric propulsion aircraft: A model predictive control approach. *IEEE Transactions on Transp. Electrification* **7(4)**, 3006–3020 (2021).

35. Yu, J. & Kim, Y. Fault-tolerant rs-lqr based yaw control for distributed electric propulsion aircraft. *2024 24th Int. Conf. on Control. Autom. Syst.* **Jeju, Korea, Republic of**, 748–749 (2024).

36. Ali, M. & Khan, O. A review of aerodynamic flow control utilizing distributed electric propulsion. *2024 4th Int. Conf. on Digit. Futur. Transform. Technol.* **Islamabad, Pakistan**, 1–9 (2024).

37. Yuan, C. *et al.* Consensus-based powered cruise and yaw controls for unmanned aerial vehicle with distributed electric propulsion system. *IEEE J. Emerg. Sel. Top. Power Electron.* **13(2)**, 1769–1782 (2025).

38. Song, Z., Feng, C., Gao, Y., Zhou, L. & Chen, Y. Fault tolerance control for asymmetric failure of distributed electric propulsion systems. *2024 3rd Int. Symp. on Aerosp. Eng. Syst.* **Nanjing, China**, 243–246 (2024).

39. Dong, Z., Li, Y., Zheng, W., Zhou, C. & Wu, P. Optimization control for aircraft based on manifold theory. *J. Aircr.* **55(6)**, 2549–2553 (2024).

40. Goran, O., Dijana, D., Dorde, V. & Bosko, R. Contemporary frame of measurement and assessment of wind-tunnel flow quality in a low-speed facility. *FME Trans* **46(4)**, 429–442 (2018).

41. Goran, O., Bosko, R. & Mirko, K. Supporting system interference on aerodynamic characteristics of an aircraft model in a low-speed wind tunnel. *Aerosp. Sci. Technol.* **64**, 133–146 (2017).

42. Dong, Z., Li, Y. & Lv, M. Adaptive nonsingular fixed-time control for hypersonic flight vehicle considering angle of attack constraints. *Int. J. Robust Nonlinear Control.* **33(12)**, 6754–6777 (2023).